



MOF-on-MOF-derived hollow FeNi₃/N-doped carbon nanorods for efficient oxygen evolution

Dandan Chen^a, Xiangli Ji^a, Xuemei Zhou^{a,*}, Qihong Sun^a, Shaojie Xu^a, Lujiao Mao^a, Zeyi Guo^a, Jia Guan^a, Ting-Ting Li^b, Jinjie Qian^{a,*}

^a Key Laboratory of Carbon Materials of Zhejiang Province, College of Chemistry and Materials Engineering, Wenzhou University, Wenzhou, Zhejiang 325000, PR China

^b School of Materials Science and Chemical Engineering, Ningbo University, Ningbo, Zhejiang 315211, PR China

ARTICLE INFO

Keywords:

MOF-on-MOF
Carbon nanomaterial
FeNi₃ alloy
Fe-doped Ni oxyhydroxide
Oxygen evolution

ABSTRACT

To achieve the carbon peak and neutrality targets, the facile synthesis of highly active and robust catalysts for efficient oxygen evolution reaction (OER) is urgently demanded. Herein, a series of metal–carbon nanomaterials (FeNi₃-NC-T, T = 600–1000 °C) with the hollow N-doped carbon nanorod incorporated FeNi₃ nanoparticles are reasonably prepared via balancing epitaxial growth and etching rate. These synthesized OER catalysts exhibit effective synergies of multiple components, large specific surface area, high conductivity, abundant exposed active sites, and intrinsic activity enhanced by carbon confinement and interconnected nanostructure. Among them, the optimized FeNi₃-NC-700 only requires low overpotentials of 262/327 mV to reach the current density of 10/50 mA cm⁻² in an alkaline medium, which is obviously better than these control samples. Owing to the aforesaid structural virtues, it exhibits high activity and good stability, fast catalytic kinetics and easy formation of active species evidenced by *in-situ* experiments as well as theoretical calculations. This study would provide a new idea for the easy fabrication of multifunctional MOF derivatives in electrochemistry with the desired properties.

1. Introduction

Hydrogen has been considered as the cleanest alternative energy source on account of its high energy output and carbon-neutral combustion products. The electrochemical water splitting shows a promising approach for producing hydrogen, which endows with the advantages of high purity, high product yield, and environmental friendliness [1–4]. At its anode, the complex oxygen evolution reaction (OER) significantly reduces the overall splitting efficiency owing to its multi-step proton-coupled electron transfer processes with sluggish reaction kinetics [5–7]. Generally speaking, these noble metal oxides such as iridium oxide (IrO₂) and ruthenium oxide (RuO₂) are deemed ideal OER catalysts, but their rarity, preciousness and inferior stability seriously restrict their large-scale industrial applications [8]. Therefore, it is imperative to explore cost-effective, high-activity and durable OER electrocatalysts based on transition metals with large reserves.

Recently, Ni-Fe nanocomposites have been well demonstrated to be highly active OER catalysts in the alkaline medium as a result of the synergistic effects between Ni and Fe species [9–12]. The doping of Fe

could effectively optimize the electronic configurations of Ni-based substrates, thus accelerating the formation of high-valence Ni species for an improved OER [13–15]. In addition, considerable efforts have been exerted to improve the electrical conductivity and catalytic activity of Ni-Fe species integrated with carbon nanomaterials [16]. With this method, it not only increases the reaction kinetics but also contributes to structural durability by protecting the metal components from erosion or detachment during electrolysis [17]. Under these circumstances, the rational engineering of Ni-Fe alloys embedded in carbon nanostructure is of great significance for high-performance OER.

On the other hand, crystalline and versatile metal–organic frameworks (MOFs) are structurally self-assembled by metal cations and organic linkers [18–21]. The abundant carbon content as well as adjustable metal composition make them a potential template for regulating the electrocatalytic performance of MOF derivatives [22]. These MOF-derived metal-carbons are inherently preserved with high conductivity and large specific surface area, which are conducive to their applications in the field of electrochemistry [23]. At present, there are various methods to promote their OER activity, such as heterometal

* Corresponding authors.

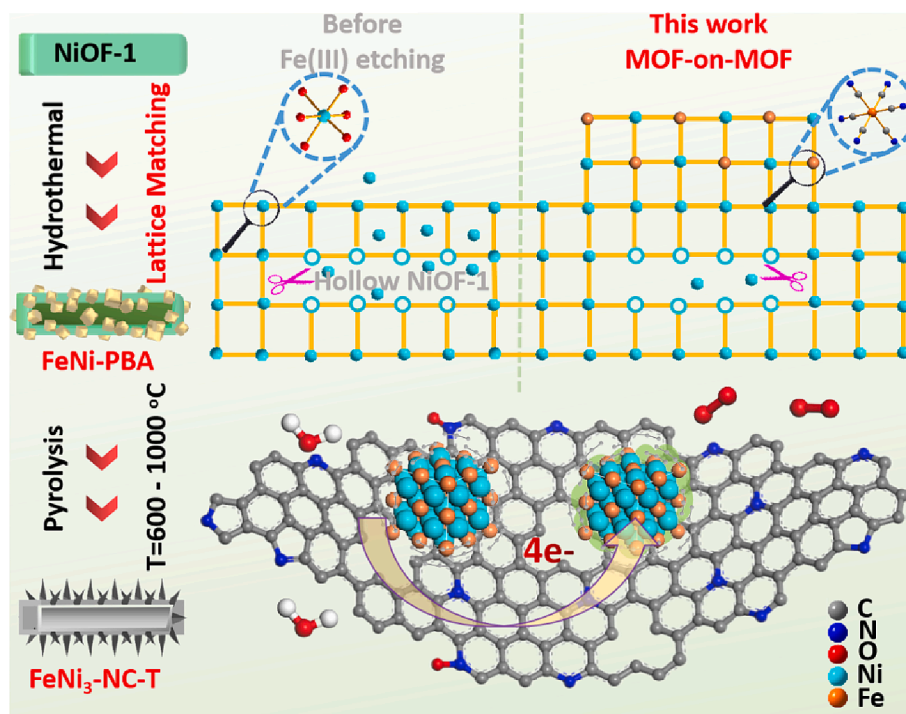
E-mail addresses: xzm.mei@163.com (X. Zhou), jinjieqian@wzu.edu.cn (J. Qian).

<https://doi.org/10.1016/j.cej.2023.144418>

Received 24 April 2023; Received in revised form 17 June 2023; Accepted 25 June 2023

Available online 26 June 2023

1385-8947/© 2023 Elsevier B.V. All rights reserved.



Scheme 1. Schematic illustration of the facile synthesis of hollow FeNi-PBA and its derived FeNi₃-NC-T series.

atom doping and morphology engineering [24]. The integration of different MOFs to obtain multiple MOF-on-MOF heterostructure is also confirmed to be a viable approach. First, the heterogeneous structure of metal centers and organic ligands alternately connected in MOF-on-MOF prevents the serious agglomeration of metal nanoparticles during pyrolysis as well as long-term electrochemical operation [25]. Meanwhile, the metal-carbon composites obtained by thermal decomposition using MOF-on-MOF templates can not only introduce the expected catalytic active substances but also easily acquire the ideal morphology [26]. By this means, these precursors with abundant heterostructures and multifunctional compositions can facilitate the subsequent catalytic performance. Above, the construction of novel MOF-on-MOF heterostructures for heterogeneous electrocatalysis has gradually become a research hotspot.

In this work, the hollow FeNi-PBA nanorod and its calcined carbon structures are systematically explored in Scheme 1. The rod-shaped NiOF-1 is first prepared as an ideal template for facile construction of MOF-on-MOF heterostructures. Different from the previous etching, the coordination bonds in NiOF-1 are easily decomposed due to the stinging hydrolysis of Fe(III), thus hollow NiOF-1 could be easily formed [27–28]. Herein, Fe(CN)₆³⁻ complex ion reacts with the *in-situ* released Ni(II) ions which leads to the fabrication of hollow MOF-on-MOF with specific morphology and crystal structure. After pyrolysis, a series of MOF-derived hollow FeNi₃-NC-T series are successfully obtained by carbonizing FeNi-PBA composites at gradient temperatures. Among them, the as-obtained electrocatalyst of FeNi₃-NC-700 with *in-situ* catalytic carbon nanotube modified and hollow nanostructures shows better electrochemical OER performance than these counterparts.

2. Results and discussion

Structurally speaking, NiOF-1 consists of half a Ni(II) ion, half a μ_2 -O anion, and one quarter of BPTC⁴⁻ in its asymmetric unit (Fig. S1a, Table S1). In Fig. S1b, each Ni(II) is 6-coordinated with an octahedron to give the {Ni₂(μ_2 -H₂O)₂(COO)₄}_n chain, and further cooperates with organic ligands to build tetragonal nanochannels of 15.3 Å (Fig. 1a, S1c). On the other hand, Pure-PBA is composed of cyano groups and

bimetal cations (Fe and Ni) in Fig. 1b. In this case, the spacing of Ni-Fe-Ni (~10.17 Å) in PBA is close to that of the four neighboring Ni atoms (~9.44 Å) in Ni-MOF, which provides a prerequisite to the formation of heterostructures (Fig. 1c) [29–31]. In Fig. 1d–e, S2–3, SEM and optical images show these green nanorods with smooth surfaces for NiOF-1, and the homogeneous Pure-PBA nanocubes exhibit a high crystallinity. Interestingly, the surface of NiOF-1 is uniformly grafted with dense PBA to produce a binary PBA-on-NiOF-1, which owns a hollow morphology during the epitaxial growth process (Fig. 1f, S4). The PXRD patterns of single MOFs are of high purity, while the peaks of FeNi-PBA at 8.3°, 9.3°, 14.9°, 16.5° and 17.2°, 24.5°, 34.8° could be assigned to (110), (101), (211), (220) crystal planes of NiOF-1 (CCDC 1014611) and (200), (220), (400) planes of Pure-PBA (PDF#86–0501), respectively, which proves the coexistence of two MOFs (Fig. 1g). Furthermore, both peaks of –COO (1559 and 1375 cm⁻¹) and –C–H (790–650 cm⁻¹) of NiOF-1, and C≡N (2081 cm⁻¹) of PBA are detected in Fig. 1h. More details on the N₂ isotherms and the corresponding pore size distribution curves of all MOF materials, please refer to Figure S5, Table S2.

The chemical conversion strategy of FeNi-PBA anchoring onto NiOF-1 precursor is clearly illustrated in Fig. 2a. Owing to the introduction of [Fe(CN)₆]³⁻, FeNi-based PBA layers can be effectively attached to the NiOF-1 nanorods with these *in-situ* released Ni(II) ions [32–33]. After that, the crystalline MOF-on-MOF gradually evolves into a hollow shape under the balanced competition coordination and etching effect. TEM images also reveal that PBA nanoparticles are grown on the surface and side of the precursor (Fig. 2b–c). The high-resolution TEM (HR-TEM) image presents the interplanar spacing of 0.36 nm corresponding to the (220) lattice plane of PBA. Furthermore, the height profile of a single FeNi-PBA verifies its hollow nanostructure (Fig. 2d), and its EDS spectrum and the corresponding elemental mappings confirm the uniform distribution of Ni, Fe, C, N and O in Fig. 2e, S6. In Fig. 2f, the TGA curve demonstrates similar thermal stability for all involved MOFs, where the early weight loss before 400 °C is reasonably attributed to the removal of solvent molecules. After 600 °C, they would be thermally converted into a series of MOF-derived porous carbon nanocomposites.

After pyrolysis, these as-obtained FeNi₃-NC-T (T = 600/700/800/

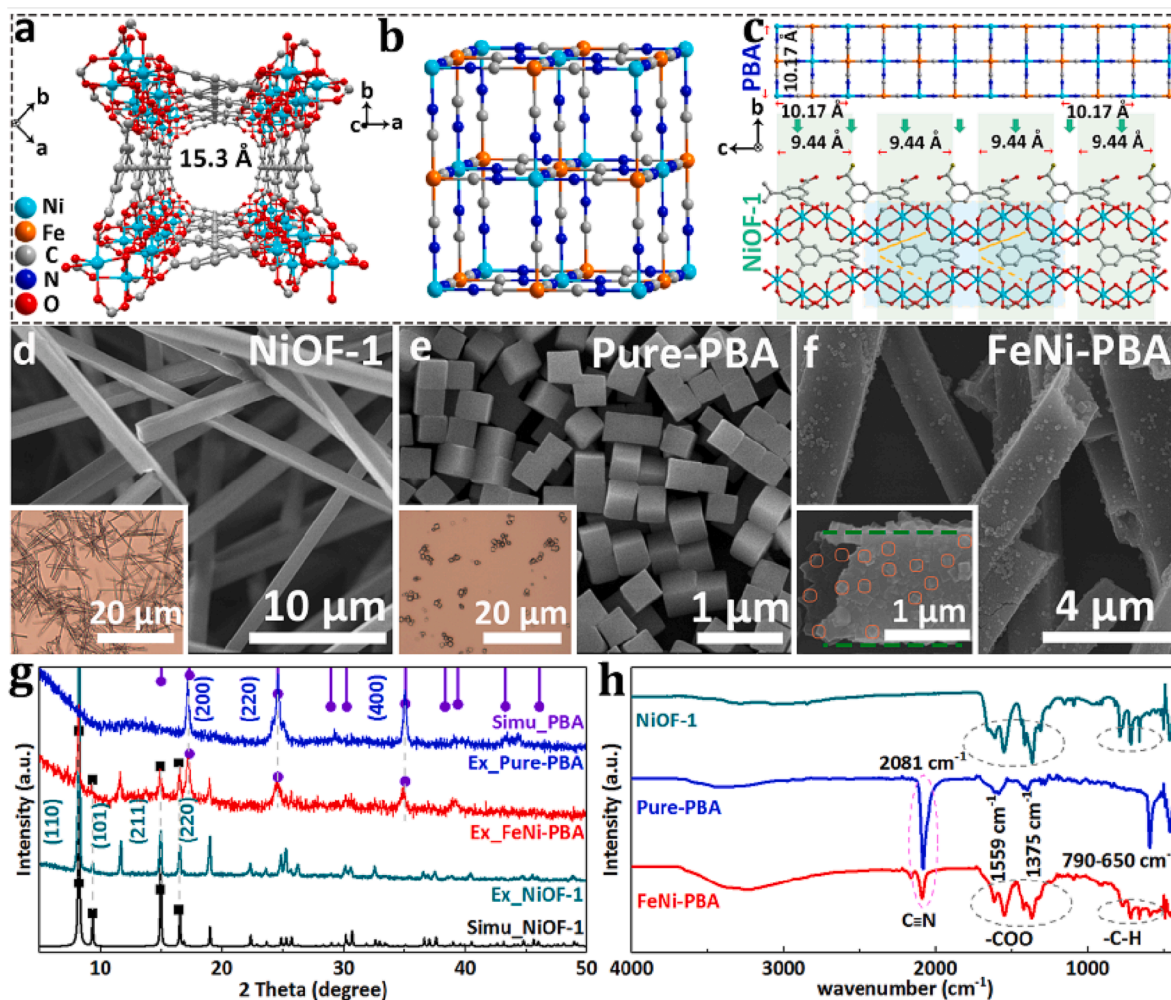


Fig. 1. Crystal structures and SEM/optical images of (a, d) NiOF-1, (b, e) Pure-PBA and (c, f) heterostructured FeNi-PBA; (g) PXRD patterns and (h) FT-IR spectra of various MOFs.

900/1000 °C) samples are featured with three main peaks of 44.3°, 51.5° and 75.9° to the (111), (200) and (220) planes for FeNi₃ (PDF#38-0419, Fig. 3a). Among them, FeNi₃-NC-700 owns the preserved rod-like nanostructure where some tiny CNTs are rooted on the surface, which is similar to other control samples in Fig. 3b-c, S7-9. Interestingly, some FeNi₃ particles are completely wrapped at the tips of CNTs with characteristic lattice fringes of 0.21 and 0.34 nm to the (111) plane of FeNi₃ and the (002) plane of graphitic carbon, respectively (Fig. 3d). In Fig. 3e, another form of FeNi₃ is also obviously observed to be coated within highly ordered carbon layers, and its lattice spacing of 0.21 nm is also consistent with the (111) crystal plane of FeNi₃. It is well known that transition metal ions could form alloys or metal nanoparticles during the carbothermic reduction process as a result of the atom movement and self-aggregation to generate nanopores at high temperatures (Figure S10) [34]. Meanwhile, the HAADF-STEM image and its elemental mappings further verify the even distribution of Ni, Fe and C elements in FeNi₃-NC-700 (Fig. 3f, S11-14).

X-ray photoelectron spectroscopy (XPS) confirms that FeNi₃-NC-700 consists of Ni, Fe, C, N and O consistent with the element mapping images. The deconvoluted Ni 2p spectra show two narrow peaks at 852.6/869.6 eV to metallic Ni(0), and two pairs of broader peaks at 855.5/872.6 eV and 861.2/879.4 eV come from the main and satellite peaks of oxidized Ni^{2+/3+}. In Fig. 4a, a slight negative shift of Ni 2p peak (0.6 eV) for FeNi₃-NC-700 compared to Ni-NC-700, which is probably attributed to the electron-density interactions after the introduction of Fe. It would significantly facilitate the electron transport between OH⁻ and catalysts,

thereby boosting the electrocatalytic activity [35]. The high-resolution Fe 2p spectrum exhibits the coexistence of metallic Fe(0) and Fe^{2+/3+} (Figure S15). The broad peak of N 1s spectra give four peaks at 398.3, 400.2, 401.0 and 403.3 eV corresponding to pyridinic, pyrrolic, graphitic and oxidized N species in Fig. 4b, respectively, while the C 1s and O 1s spectra are shown in Figure S15c-d. Furthermore, Raman curves display two peaks at 1350 and 1580 cm⁻¹ for amorphous sp³ (D band) and graphitic sp² (G band) carbon, respectively. Among them, FeNi₃-NC-700 owns a moderate I_D/I_G ratio of 1.01 with a suitable degree of graphitization, which would accelerate the electron transfer during electrocatalysis (Fig. 4c) [36]. Finally, the BET surface areas and pore sizes of these MOF-derived carbon nanomaterials are depicted in Figure S16 and Table S2.

The OER performance is first evaluated by LSV curves where FeNi₃-NC-700 exhibits a decent performance with low overpotential values (η_{10/50}) of 262/327 mV to achieve 10/50 mA cm⁻². It is superior to those of FeNi₃-NC-600/800/900/1000 (294/366, 288/356, 328/437, 332/461 mV), Ni-NC-700 (381/512 mV), Pure-PBA-NC-700 (340/444 mV) and RuO₂ (291/404 mV) in Fig. 5a-b, S17. Its enhanced catalytic activity is also supported by the lowest Tafel slope of 69.4 mV dec⁻¹, smaller than those control materials (Fig. 5c). The electrochemically active surface area (ECSA) based on the double-layer capacitance (C_{dl}) shows that FeNi₃-NC-700 (8.42 mF cm⁻²) is prominently larger for its hierarchically porous nanostructure (Fig. 5d, S18-19). In contrast, the current intensity for FeNi₃-NC-900/1000 decreases significantly, which stems from reduced specific surface area by serious aggregation of FeNi

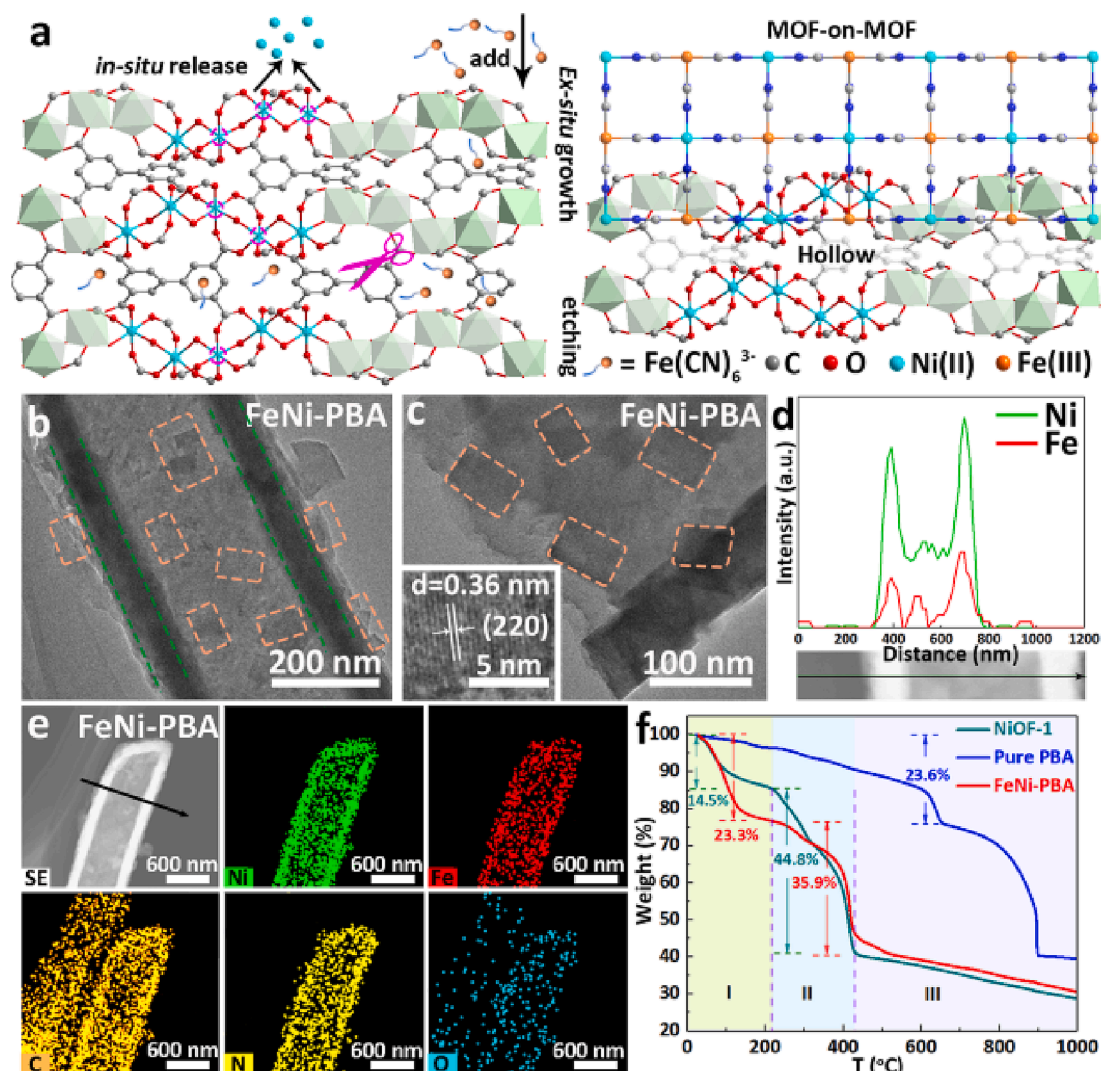


Fig. 2. (a) Schematic preparation of FeNi-PBA; (b-c) TEM and HR-TEM images, (d) the height profile, (e) HAADF-STEM and element mapping images of FeNi-PBA; (f) TGA curves of NiOF-1, Pure-PBA and FeNi-PBA.

alloys [37–38]. In Fig. 5e, the EIS result of FeNi₃-NC-700 shows a semicircle radius comparable to that of RuO₂, testifying the rapid reaction kinetics. Furthermore, the rotating ring-disk electrode (RRDE) is used to detect the number of electrons (N) transferred to each O₂, where the ring current (I_{ring}) is almost negligible compared with the disk current (I_{disk}). Herein, the average N value is calculated to be 3.9 to infer the quasi-four-electron process (Fig. 5f). Subsequently, near 100% Faraday efficiency is also recorded to suggest that oxidation current is intrinsically generated by oxygen evolution (Figure S20). Besides, its durability is measured by i-t curve in Fig. 5g, which retains the current retention rate of 93.2%/81.5% over 10/ 50 h (Figure S21), and there is almost no obvious current loss after 500 cycles. In order to further assess the stability of our material, we conducted SEM and TEM tests on the samples after prolonged measurements. SEM characterization of samples subjected to long-term durability tests reveals that the structure of FeNi₃-NC-700 remains substantially intact with minimal collapse (Figure S22). Additionally, in the TEM images (Figure S23), FeNi₃ nanoparticles in the FeNi₃-NC-700 material after the OER are observed to be partially reduced and slightly agglomerated, which understandably leads to reduced performance. In the PXRD test, samples after the OER test exhibit three main peaks consistent with FeNi₃ (Figure S24). As shown in Figure S25a, the obtained XPS spectra reveal five elements: C, N, O, Fe, and Ni, confirming that the elemental composition of FeNi₃-

NC-700 remains unchanged after the OER cycle test. Furthermore, in the Ni 2p region (Figure S25b), the XPS analysis demonstrates a shift to higher binding energy for the Ni(II/III) peaks and a weakening of the Ni (0) peaks after the long-term OER process. A similar situation is observed in the Fe 2p spectrum (Figure S25c), where the Fe(II/III) peak shifts to higher binding energy and the Fe(0) peak is weakened as well. These features indicate partial surface oxidation of FeNi₃-NC-700 during the OER process. In Table S3, the TOF value of FeNi₃-NC-700 ($6.38 \times 10^{-3} \text{ s}^{-1}$) is much higher than that of Ni-NC-700 ($2.52 \times 10^{-4} \text{ s}^{-1}$) and Pure-PBA-NC-700 ($7.82 \times 10^{-4} \text{ s}^{-1}$) at an overpotential of 300 mV, and roughly 2-fold higher than that of RuO₂ ($3.18 \times 10^{-3} \text{ s}^{-1}$). More importantly, it shows competitive OER properties in comparison with those previous electrocatalysts in Fig. 5h and Table S4-S5.

It exhibits a gradually increasing and finally stabilizing trend from the activation of the catalyst in the OH-rich medium after 10 cycles (Fig. 6a, S26) [39]. Meanwhile, the structural reconstruction of FeNi₃ towards oxidized Fe-doped NiOOH species is explored through *in-situ* EIS measurements, showing an increase in impedance (Fig. 6b). In Fig. 6c, Raman spectroscopy is also adopted to reveal the active species of FeNi₃-NC-700 at the working conditions. Before OER, a distinct peak at 480 cm^{-1} is reasonably assigned to stretching modes of FeNi-O for FeNi₃-NC-700. When it commences at 1.25 V (vs. SCE), some weak peaks at 580 and 900 cm^{-1} are observed from the vibration of FeNiOOH

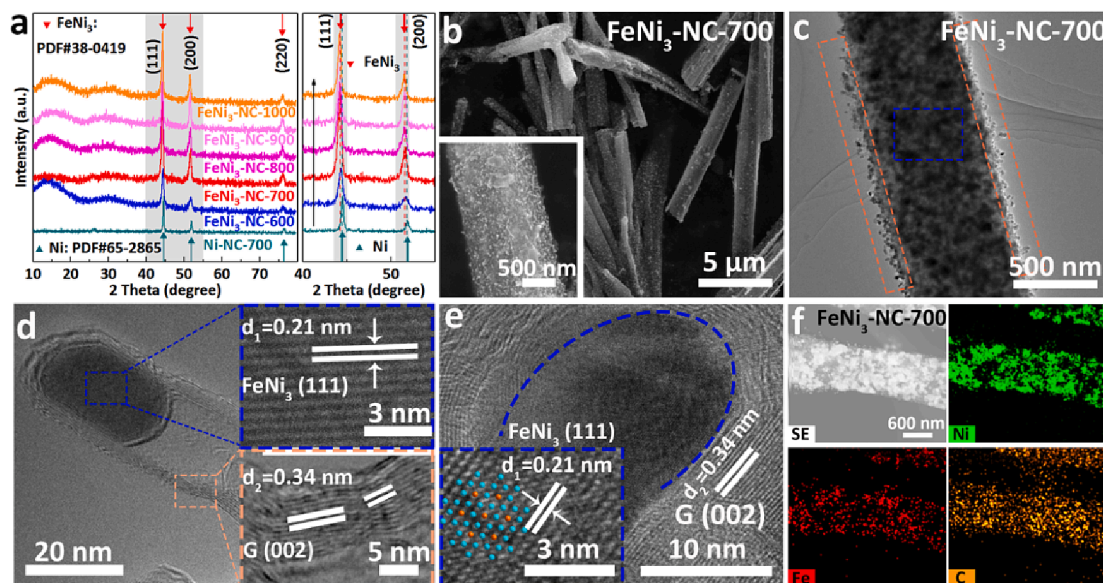


Fig. 3. (a) PXRD patterns of Ni-NC-700 and FeNi₃-NC-T series; (b, c, d-e) SEM, TEM, and HR-TEM images, (f) HAADF-STEM and element mapping images of FeNi₃-NC-700.

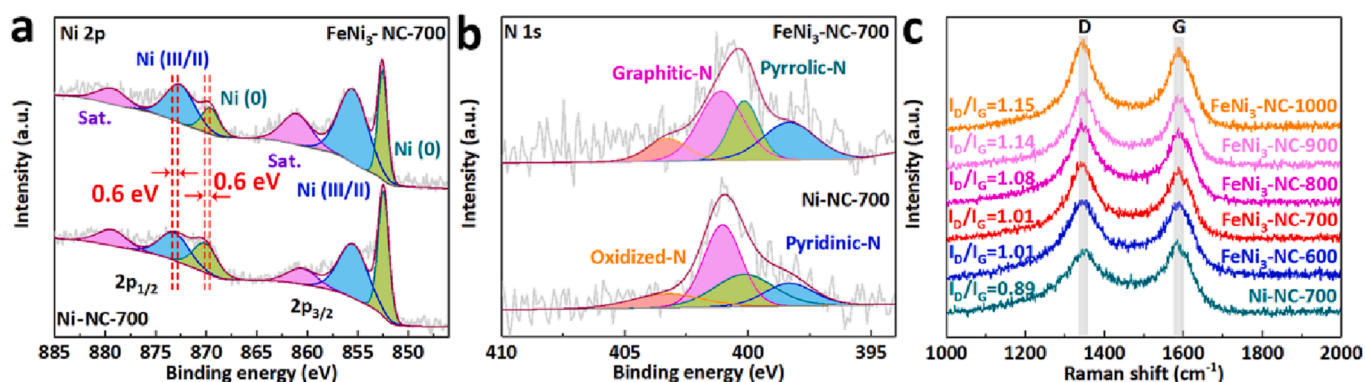


Fig. 4. The high-resolution XPS spectra of (a) Ni 2p and (b) N 1s for FeNi₃-NC-700 and Ni-NC-700; (c) Raman spectra of Ni-NC-700 and FeNi₃-NC-T series.

(Figure S27). After OER, the amorphous integrated with crystalline counterparts could enhance the electrocatalytic activities owing to their enriched active sites as compared to pure crystalline counterparts in Fig. 6d-e, S28 [40]. The overall OER pathways on FeNiOOH/FeNi₃ are depicted in Fig. 6f, S29-31 [41-43]. First of all, one H₂O molecule is adsorbed on Ni (0.31 eV), which is closest to doping-Fe (State 1). The first oxidation takes place in the deprotonation of the hydrogen bond on the bridging O between adjacent Ni centers (1.17 eV, State 2). Followed by that is the deprotonation of H₂O adsorbed on a neighboring Ni (0.87 eV, State 3). The third step is normally the rate-determining step that generates an O radical (O[•]) through deprotonation of the OH adsorbed on Ni closest to doping-Fe with an additional H₂O (1.67 eV, State 4). The formed O[•] promotes the coupling of O-O and H₂O to form OOH (-0.16 eV, State 4'). The fourth oxidation step with deprotonation of the OOH is carried out in State 4', which requires 0.81 eV to generate superoxide in State 5. It returns to the starting point (State 0) after releasing O₂ molecule through a non-electrochemical charge transfer step (0.39 eV).

3. Conclusion

In summary, a series of hollow carbon nanostructures with abundant FeNi₃ nanoparticles have been conveniently prepared by a MOF-on-MOF strategy. The as-obtained catalysts of FeNi₃-NC-T well exhibit a

multi-component positive synergy, such as ordered graphitic carbon layers incorporated FeNi₃ nanoparticles, large active sites and increased intrinsic activity, which are confirmed by the physical characterization and electrochemical tests. Specifically, the obtained FeNi₃-NC-700 shows a superior OER performance with low overpotential values of 262 mV and 327 mV to achieve the current density of 10 mA cm⁻² and 50 mA cm⁻², a Tafel slope as low as 69.4 mV dec⁻¹, and a current retention rate of 93.2% after 10 h. In general, these hollow carbon nanotubes with self-catalyzed hierarchical nanostructure promote the synergistic effect of active site exposure and shorten the electron transfer path, while Fe-doped nickel hydroxide enhances the intrinsic activity during OER. Above, this work demonstrates a facile way to explore the heterogeneous catalysis of MOF-on-MOF derived nanomaterials which is widely used in energy-related applications.

Author contributions

JJ Qian conceived the research project. DD Chen conducted the experiments, performed the characterizations, and wrote the manuscript. XM Zhou revised the main article. All authors have checked and given approval to the final version of the manuscript.

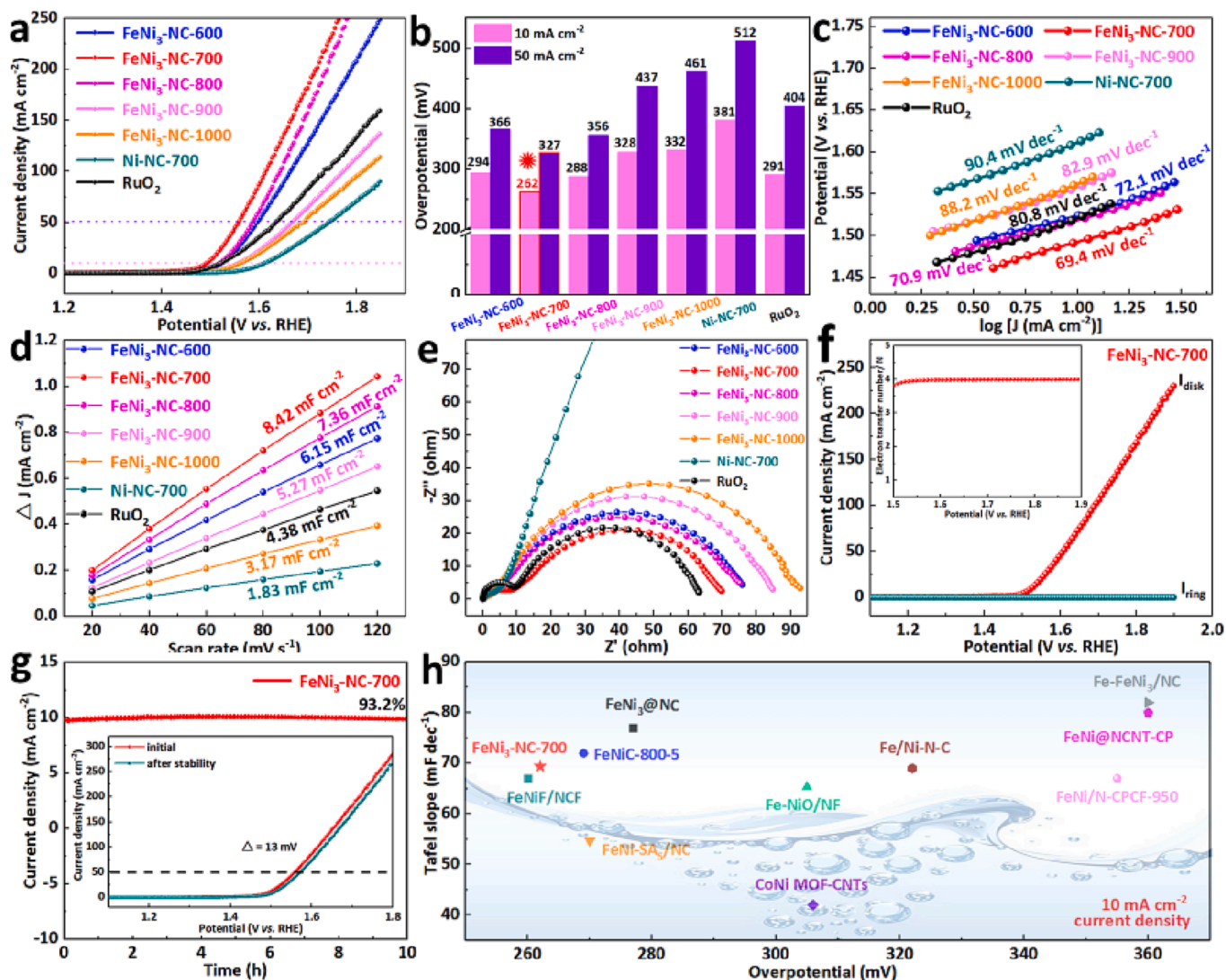


Fig. 5. (a) LSV curves, (b) electrochemical $\eta_{10/50}$ comparison, (c) Tafel plots, (d) Cdl values, (e) EIS diagram of Ni-NC-700, FeNi₃-NC-T and RuO₂; (f) RRDE voltammogram and its calculated N, (g) the stability evaluation of FeNi₃-NC-700; (h) OER comparison with those reported electrocatalysts.

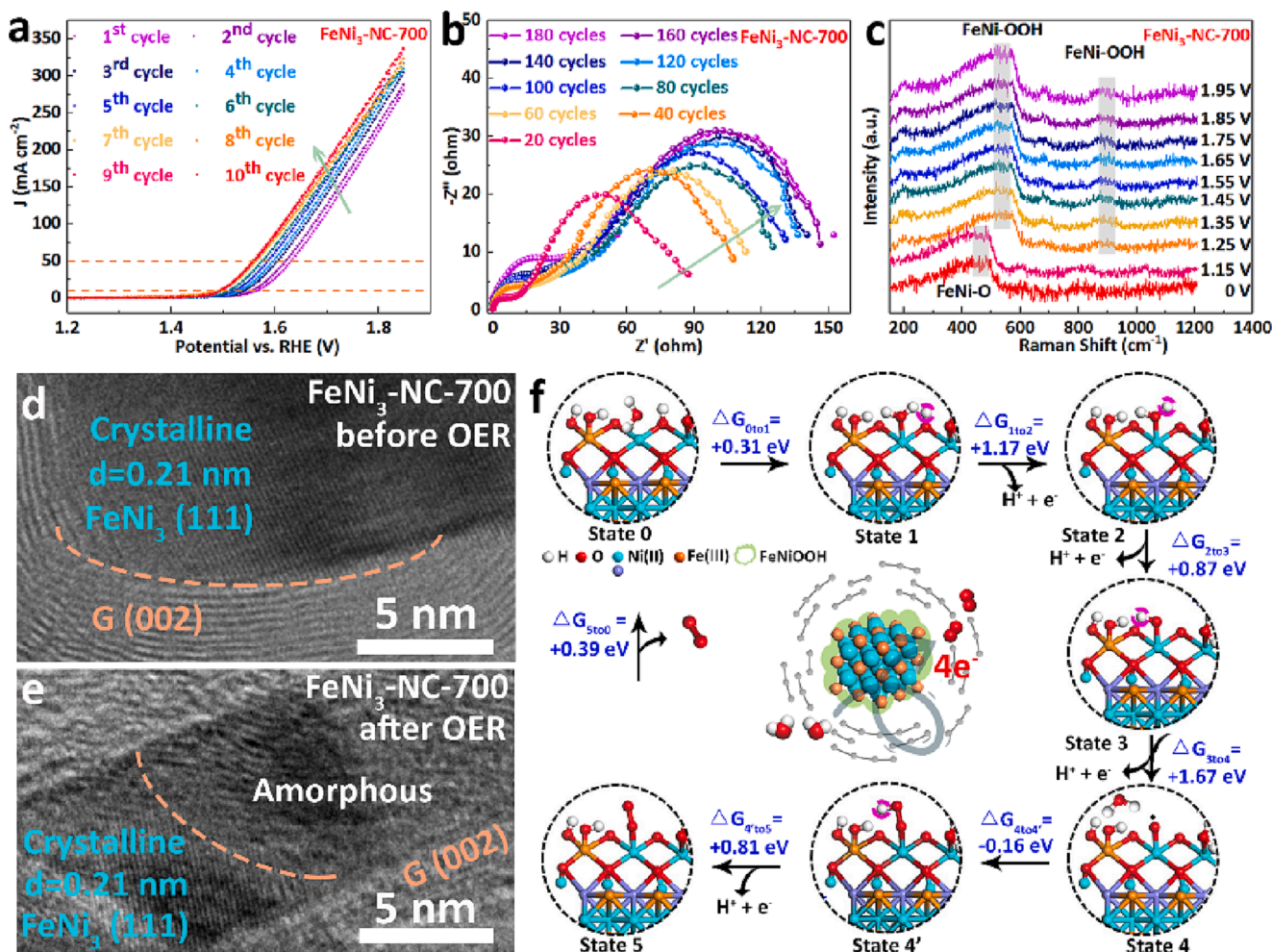


Fig. 6. (a) LSV trends in the first 10 cycles, (b) *in-situ* EIS curves, (c) *in-situ* Raman spectra; (d-e) HR-TEM images of FeNi₃-NC-700 before/after OER; (f) Mechanism for OER on the optimized Ni_{1-x}Fe_xOOH/FeNi₃.

Declaration of Competing Interest

The authors declare that they have no known competing financial interests or personal relationships that could have appeared to influence the work reported in this paper.

Data availability

Data will be made available on request.

Acknowledgments

This work was financially supported by National Natural Science Foundation of China (21601137), Natural Science Foundation of Zhejiang Province (LQ16B010003), Basic Science and Technology Research Project of Wenzhou, Zhejiang Province (H20220001), and the Special Basic Cooperative Research Programs of Yunnan Provincial Undergraduate Universities Association (202101BA070001-042).

Appendix A. Supplementary data

Supplementary data to this article can be found online at <https://doi.org/10.1016/j.cej.2023.144418>.

References

- [1] Y. Jiao, Y. Zheng, M. Jaroniec, S.Z. Qiao, Design of electrocatalysts for oxygen- and hydrogen-involving energy conversion reactions, *Chem. Soc. Rev.* 44 (8) (2015) 2060–2086.
- [2] A. Sahasrabudhe, H. Dixit, R. Majee, S. Bhattacharyya, Value added transformation of ubiquitous substrates into highly efficient and flexible electrodes for water splitting, *Nat. Commun.* 9 (1) (2018) 2014.
- [3] J. Kang, X. Qiu, Q. Hu, J. Zhong, X. Gao, R. Huang, C. Wan, L.-M. Liu, X. Duan, L. Guo, Valence oscillation and dynamic active sites in monolayer NiCo hydroxides for water oxidation, *Nat. Catal.* 4 (12) (2021) 1050–1058.
- [4] Q.i. Yan, X. Duan, Y. Liu, F. Ge, H. Zheng, A hybridization cage-confinement pyrolysis strategy for ultrasmall Ni₃Fe alloy coated with N doped carbon nanotubes as bifunctional oxygen electrocatalysts for Zn-air batteries, *J. Mater. Chem. A* 11 (3) (2023) 1430–1438.
- [5] N. Zhang, Y. Chai, Lattice oxygen redox chemistry in solid-state electrocatalysts for water oxidation, *Energy Environ. Sci.* 14 (9) (2021) 4647–4671.
- [6] X. Su, Y. Wang, J. Zhou, S. Gu, J. Li, S. Zhang, Operando spectroscopic identification of active sites in NiFe prussian blue analogues as electrocatalysts: activation of oxygen atoms for oxygen evolution reaction, *J. Am. Chem. Soc.* 140 (36) (2018) 11286–11292.
- [7] W. Wang, Z. Wang, Y. Hu, Y. Liu, S. Chen, A potential-driven switch of activity promotion mode for the oxygen evolution reaction at Co₃O₄/NiO_xH_y interface, *eScience* 2 (4) (2022) 438–444.
- [8] N. Li, L. Cai, C. Wang, Y. Lin, J. Huang, H. Sheng, H. Pan, W. Zhang, Q. Ji, H. Duan, W. Hu, W. Zhang, F. Hu, H. Tan, Z. Sun, B. Song, S. Jin, W. Yan, Identification of the active-layer structures for acidic oxygen evolution from 9R-BaIrO₃ electrocatalyst with enhanced iridium mass activity, *J. Am. Chem. Soc.* 143 (43) (2021) 18001–18009.
- [9] X. Zhang, X. Fang, K. Zhu, W. Yuan, T. Jiang, H. Xue, J. Tian, Fe-doping induced electronic structure reconstruction in Ni-based metal-organic framework for improved energy-saving hydrogen production via urea degradation, *J. Power Sources* 520 (2022), 230882.

- [10] D. Li, H. Liu, L. Feng, A Review on advanced FeNi-based catalysts for water splitting reaction, *Energy Fuels* 34 (11) (2020) 13491–13522.
- [11] Y. Guo, C. Zhang, J. Zhang, K. Dastafkan, K. Wang, C. Zhao, Z. Shi, Metal-organic framework-derived bimetallic NiFe selenide electrocatalysts with multiple phases for efficient oxygen evolution reaction, *ACS Sustainable Chem. Eng.* 9 (5) (2021) 2047–2056.
- [12] W. Zhao, H. Xu, H. Luan, N. Chen, P. Gong, K. Yao, Y. Shen, Y. Shao, NiFe Layered double hydroxides grown on a corrosion-cell cathode for oxygen evolution electrocatalysis, *Adv. Energy Mater.* 12 (2) (2021) 2102372.
- [13] F. Zheng, W. Zhang, X. Zhang, Y. Zhang, W. Chen, Sub-2 nm ultrathin and robust 2D FeNi layered double hydroxide nanosheets packed with 1D FeNi-MOFs for enhanced oxygen evolution electrocatalysis, *Adv. Funct. Mater.* 31 (43) (2021) 2103318.
- [14] S. Zou, M.S. Burke, M.G. Kast, J. Fan, N. Danilovic, S.W. Boettcher, Fe (oxy) hydroxide oxygen evolution reaction electrocatalysis: intrinsic activity and the roles of electrical conductivity, substrate, and dissolution, *Chem. Mater.* 27 (23) (2015) 8011–8020.
- [15] L.i. Zhong, L. He, N.i. Wang, Y. Chen, X. Xie, B. Sun, J. Qian, S. Komarneni, W. Hu, Preparation of metal-organic framework from in situ self-sacrificial stainless-steel matrix for efficient water oxidation, *Appl. Catal., B* 325 (2023), 122343.
- [16] S. Li, Y. Gao, N. Li, L. Ge, X. Bu, P. Feng, Transition metal-based bimetallic MOFs and MOF-derived catalysts for electrochemical oxygen evolution reaction, *Energy Environ. Sci.* 14 (4) (2021) 1897–1927.
- [17] L. Jiao, G. Wan, R. Zhang, H. Zhou, S.-H. Yu, H.-L. Jiang, From metal-organic frameworks to single-atom Fe implanted N doped porous carbons: efficient oxygen reduction in both alkaline and acidic media, *Angew. Chem., Int. Ed.* 57 (28) (2018) 8525–8529.
- [18] Ren, S.; Duan, X. Ge, F.; Chen, Z.; Yang, Q. Zhang, M.; Zheng, H., Novel MOF-derived hollow CoFe alloy coupled with N-doped Ketjen Black as boosted bifunctional oxygen catalysts for Zn-air batteries. *Chem. Eng. J.* 2022, 427 (1), 131614.
- [19] C. Cao, D.-D. Ma, Q. Xu, X.-T. Wu, Q.-L. Zhu, Semisacrificial template growth of self-supporting MOF nanocomposite electrode for efficient electrocatalytic water oxidation, *Adv. Funct. Mater.* 29 (6) (2019) 1807418.
- [20] H.C. Zhou, S. Kitagawa, Metal-organic frameworks (MOFs), *Chem. Soc. Rev.* 43 (16) (2014) 5415–5418.
- [21] Liu, P.; Liu, A.; Wang, P.; Chen, Y.; Li, B., Smart crystalline frameworks constructed with bisquinoline-based component for multi-stimulus luminescent sensing materials. *Chin. J. Struct. Chem.* 2023, 42, 100001.
- [22] F.L. Li, Q. Shao, X. Huang, J.P. Lang, Nanoscale trimetallic metal-organic frameworks enable efficient oxygen evolution electrocatalysis, *Angew. Chem., Int. Ed.* 57 (7) (2018) 1888–1892.
- [23] Z. Li, M. Song, W. Zhu, W. Zhuang, X. Du, L. Tian, MOF-derived hollow heterostructures for advanced electrocatalysis, *Coord. Chem. Rev.* 439 (2021), 213946.
- [24] H.F. Wang, L. Chen, H. Pang, S. Kaskel, Q. Xu, MOF-derived electrocatalysts for oxygen reduction, oxygen evolution and hydrogen evolution reactions, *Chem. Soc. Rev.* 49 (5) (2020) 1414–1448.
- [25] Y. Zhou, H. Liu, X. Gu, X. Wu, L. Feng, Hetero MOF-on-MOF-derived carbon nanotube interconnected nitrogen-doped carbon-encapsulated FeNi/FeF₂ for efficient oxygen evolution reaction, *Carbon Energy* 4 (5) (2022) 924–938.
- [26] L. Mao, D. Chen, Y. Guo, C. Han, X. Zhou, Z. Yang, S. Huang, J. Qian, Different growth behavior of MOF-on-MOF heterostructures to enhance oxygen evolution, *ChemSusChem* 16 (1) (2023) e202201947.
- [27] D. Chen, Q. Sun, C. Han, Y. Guo, Q. Huang, W.A. Goddard, J. Qian, Enhanced oxygen evolution catalyzed by in situ formed Fe-doped Ni oxyhydroxides in carbon nanotubes, *J. Mater. Chem. A* 10 (30) (2022) 16007–16015.
- [28] X. Wang, L. Chai, J. Ding, L. Zhong, Y. Du, T.-T. Li, Y. Hu, J. Qian, S. Huang, Chemical and morphological transformation of MOF-derived bimetallic phosphide for efficient oxygen evolution, *Nano Energy* 62 (2019) 745–753.
- [29] X. Zhang, W. Chen, W. Shi, P. Cheng, Highly selective sorption of CO₂ and N₂O and strong gas-framework interactions in a nickel(ii) organic material, *J. Mater. Chem. A* 4 (41) (2016) 16198–16204.
- [30] J. Qian, F. Jiang, D. Yuan, M. Wu, S. Zhang, L. Zhang, M. Hong, Highly selective carbon dioxide adsorption in a water-stable indium-organic framework material, *Chem. Commun.* 48 (78) (2012) 9696–9698.
- [31] W. Ahn, M.G. Park, D.U. Lee, M.H. Seo, G. Jiang, Z.P. Cano, F.M. Hassan, Z. Chen, Hollow multivoid nanocuboids derived from ternary Ni-Co-Fe prussian blue analog for dual-electrocatalysis of oxygen and hydrogen evolution reactions, *Adv. Funct. Mater.* 28 (28) (2018) 1802129.
- [32] S. Lee, S. Oh, M. Oh, Atypical hybrid metal-organic frameworks (MOFs): a combinative process for MOF-on-MOF growth, etching, and structure transformation, *Angew. Chem., Int. Ed.* 59 (3) (2020) 1327–1333.
- [33] C. Liu, J. Wang, J. Wan, C. Yu, MOF-on-MOF hybrids: Synthesis and applications, *Coord. Chem. Rev.* 432 (2021), 213743.
- [34] C. Wang, J. Kim, J. Tang, M. Kim, H. Lim, V. Malgras, J. You, Q. Xu, J. Li, Y. Yamauchi, New Strategies for novel MOF-derived carbon materials based on nanoarchitectures, *Chem.* 6 (1) (2020) 19–40.
- [35] J. Zhao, J.-J. Zhang, Z.-Y. Li, X.-H. Bu, Recent progress on NiFe-based electrocatalysts for the oxygen evolution reaction, *Small* 16 (51) (2020) e2003916.
- [36] Z. Liu, X. Yu, H. Yu, H. Xue, L. Feng, Nanostructured FeNi₃ incorporated with carbon doped with multiple nonmetal elements for the oxygen evolution reaction, *ChemSusChem* 11 (16) (2018) 2703–2709.
- [37] L. Yang, X. Zeng, D. Wang, D. Cao, Biomass-derived FeNi alloy and nitrogen-codoped porous carbons as highly efficient oxygen reduction and evolution bifunctional electrocatalysts for rechargeable Zn-air battery, *Energy Storage Mater.* 12 (2018) 277–283.
- [38] J. Ding, Q. Sun, L.i. Zhong, X. Wang, L. Chai, Q. Li, T.-T. Li, Y. Hu, J. Qian, S. Huang, Thermal conversion of hollow nickel-organic framework into bimetallic FeNi₃ alloy embedded in carbon materials as efficient oer electrocatalyst, *Electrochim. Acta* 354 (2020), 136716.
- [39] A. Dutta, N. Pradhan, Developments of metal phosphides as efficient OER precatalysts, *J. Phys. Chem. Lett.* 8 (1) (2017) 144–152.
- [40] Z. Gong, R. Liu, H. Gong, G. Ye, J. Liu, J. Dong, J. Liao, M. Yan, J. Liu, K. Huang, L. Xing, J. Liang, Y. He, H. Fei, Constructing a graphene-encapsulated amorphous/crystalline heterophase NiFe alloy by microwave thermal shock for boosting the oxygen evolution reaction, *ACS Catal.* 11 (19) (2021) 12284–12292.
- [41] Shin, H.; Xiao, H.; Goddard, W. A., 3rd, In silico discovery of new dopants for Fe-doped Ni oxyhydroxide (Ni_{1-x}Fe_xOOH) catalysts for oxygen evolution reaction. *J. Am. Chem. Soc.* 2018, 140 (22), 6745–6748.
- [42] F.L. Li, P. Wang, X. Huang, D.J. Young, H.F. Wang, P. Braunstein, J.P. Lang, Large-scale, bottom-up synthesis of binary metal-organic framework nanosheets for efficient water oxidation, *Angew. Chem. Int. Ed. Engl.* 58 (21) (2019) 7051–7056.
- [43] C. Kuai, C. Xi, A. Hu, Y. Zhang, Z. Xu, D. Nordlund, C.-J. Sun, C.A. Cadigan, R. M. Richards, L. Li, C.-K. Dong, X.-W. Du, F. Lin, Revealing the dynamics and roles of iron incorporation in nickel hydroxide water oxidation catalysts, *J. Am. Chem. Soc.* 143 (44) (2021) 18519–18526.